Materials Advances

ROYAL SOCIETY OF CHEMISTRY

PAPER

View Article Online
View Journal | View Issue

Cite this: *Mater. Adv.*, 2026, 7, 3166

Studies on the structural, microstructure, dielectric, electrical and optical properties of Gd-doped $BiFeO_3$ ceramic and its NTC thermistor application

Swati Panda and S. K. Parida *

This study presents a comprehensive investigation of Gd-doped $BiFeO_3$ [$Bi_{0.9}Gd_{0.1}FeO_3$, BGFO] ceramics synthesized *via* a conventional solid-state reaction method. The preliminary structural Rietveld analysis confirms the formation of a rhombohedral structure (#$R\bar{3}c$) with an average crystallite size of 65.5 nm, a micro-lattice strain of 0.00106, and a dislocation density of 2.33×10^{14} m^{-2}. The analysis of the FTIR spectrum confirms the presence of all atomic vibration bands in the studied sample. The analysis of UV visible data shows a wide bandgap energy of 2.9 eV, which may be suitable for applications in photodetectors, LEDs, *etc.* The study of dielectric properties *versus* frequency and temperature reveals that the studied sample has a high dielectric constant and low loss, making the material a better candidate for energy storage devices. The study of impedance plots *versus* frequency supports the semiconducting nature of the sample. The study of modulus plots *versus* frequency confirms the non-Debye type of relaxation mechanism. The study of the ac conductivity *versus* both frequency and temperature confirms a thermally activated hopping mechanism. Both the Nyquist and Cole–Cole plots support the semiconducting nature of the sample. Additionally, the material exhibits negative temperature coefficient (NTC) thermistor behavior, confirming its potential for temperature sensor applications.

Received 13th August 2025,
Accepted 2nd February 2026

DOI: 10.1039/d5ma00885a

rsc.li/materials-advances

1. Introduction

The performance of single perovskite materials in optoelectronic applications heavily depends on their structural stability and phase purity, which are critical for achieving consistent electronic and optical properties.[1] Single perovskite materials offer tunable band gaps through compositional engineering, making them versatile for applications ranging from photovoltaics to light-emitting diodes.[2] A single perovskite is a type of material that follows a specific crystal structure, originally found in the mineral calcium titanium oxide ($CaTiO_3$). This structure is represented by the formula ABX_3, where "A" is a larger positive ion, "B" is a smaller metal ion, and "X" is a negatively charged oxygen or halide like iodide, bromide, or chloride. Single perovskite materials are widely applied in optoelectronic devices such as solar cells, light-emitting diodes (LEDs), and photodetectors due to their tunable bandgap, and in energy storage devices due to their high dielectric constant and low loss, high absorption coefficients, and excellent charge transport properties.[3–7]

Doping in single perovskite materials is important because it enables precise tuning of their electrical, magnetic, and structural properties to meet specific functional requirements. By introducing controlled impurities, researchers can enhance performance, stabilize phases, or induce new properties that are essential for advanced electronic and energy applications.[8–13] $BiFeO_3$ is one of the few single-phase multiferroic materials that exhibits both ferroelectricity and antiferromagnetism at room temperature, making it highly attractive for multifunctional devices.[14,15] Pure BFO ceramics often suffer from high leakage current due to oxygen vacancies and volatile bismuth loss during sintering, which limits their practical ferroelectric applications.[16,17] Doping $BiFeO_3$ is essential because it enables tuning of its multiferroic behavior, which is vital for oxide memory technologies and other multifunctional devices. By introducing dopants, the magnetic and ferroelectric characteristics of the material can be adjusted to achieve targeted functionalities. Doping with rare-earth or transition metal ions and reducing grain size through nanostructuring significantly improves the electrical, magnetic, and structural stability of $BiFeO_3$ ceramics.[18,19]

$BiFeO_3$ is a room-temperature multiferroic material, but its practical use is limited due to high leakage current, secondary phases, and weak magnetism. Doping with rare-earth ions like

Department of Physics, ITER, Siksha 'O' Anusandhan Deemed to be University, Bhubaneswar-751030, India. E-mail: santoshparida@soa.ac.in

Gd^{3+} (gadolinium) at the Bi-site has proven effective in enhancing its magnetoelectric performance and structural stability.[20–24] Gd^{3+} (ionic radius ~0.938 Å) has a smaller ionic size than Bi^{3+} (~1.03 Å), introducing internal chemical pressure, reducing distortion, and enhancing magnetism and dielectric properties. Taking the problem of doping Gd in the bismuth site in the $BiFeO_3$ ceramic host, the authors decided to explore the structural, dielectric, electric, and optical properties, along with searching for NTC thermistor applications.

2. Experimental details

2.1 Materials required

$Bi_{0.9}Gd_{0.1}FeO_3$ nanoparticles were synthesized using a conventional solid-state reaction method. For the synthesis of this polycrystalline compound, raw materials Bi_2O_3, Fe_2O_3, and Gd_2O_3 of AR grade with 99% purity were procured from LOBA Chemie Pvt. Ltd. The required metal oxide powders were measured stoichiometrically using an electronic digital balance [MODEL: ML204/A01] with an accuracy of 0.0001 g. The required chemical equation for the synthesis of the final product through a stoichiometric ratio is given as: $0.45Bi_2O_3 + 0.05Gd_2O_3 + 0.5Fe_2O_3 \rightarrow Bi_{0.9}Gd_{0.1}FeO_3$. This equation decides the quantity of the procured metal oxide required for the synthesis of the final product.

2.2 Sample synthesis

The metal powders were thoroughly mixed using an agate mortar and pestle in a dry medium for 3 h, followed by wet mixing for another 3 h for better homogeneity. The mixture was then calcinated at a rate of 3 °C min^{-1} for 6 h at 850 °C. The XRD pattern of the calcinated sample was recorded to confirm the formation of a stable crystal structure. Subsequently, polyvinyl alcohol (PVA) was added to the calcinated powder to prepare cylindrical pellets with a diameter of 12 mm and a thickness of 2 mm using a KBr hydraulic press under a pressure of 4.0×10^6 N m^{-2}. The pellets were sintered at 900 °C for 5 h in a muffle furnace to remove impurities of carbon and oxygen, if any, and also to make a dense material with better electrical properties.

2.3 Characterization

Structural analysis was performed at room temperature using an X-ray diffractometer [MODEL: Rigaku Ultima IV, source = Cu Kα, step size = 0.02°] over a wide range of Bragg angles ($20° \leq \theta \leq 80°$). Fourier transform infrared (PerkinElmer Model no. Spectrum Two Serial no. 105627 FT-IR) spectroscopy was used to record the FTIR spectrum of the prepared samples. To measure the bandgap energy and hence to investigate the semiconducting behavior of the proposed sample, the UV-vis spectroscopy analysis has been tailored. The UV-vis data were recorded using the MODEL: V670, being customized for source D2/WI and a bandwidth equal to 2 nm with a scan speed limit of 400 nm min^{-1}. High-temperature dielectric data were recorded using an LCR analyzer [MODEL: N4L PSM 1735] over a frequency range of 1 kHz to 1 MHz and a temperature range of 25 °C to 500 °C.

3. Results and discussion

3.1 Structure stability

To understand the stability of the Gd-doped $BiFeO_3$ ceramics, the Goldschmidt tolerance factor (t) must be evaluated. The mathematical relation for the tolerance factor can be written as: $t = \frac{(0.9R_{Bi^{3+}} + 0.1R_{Gd^{3+}}) + R_{O^{2-}}}{\sqrt{2}(R_{Fe^{3+}} + R_{O^{2-}})}$, where all symbols have their usual meaning.[25,26] The permitted value of t for a stable perovskite material should fall in the range $0.75 \leq t \leq 1.02$.[27] In the present study, the value of the tolerance factor of the BGFO ceramic is found to be 0.83, which supports the formation of a rhombohedral structure.

3.2 XRD analysis

XRD is essential for ceramic structural analysis as it identifies crystalline phases, determines the crystal structure, and assesses phase purity and lattice parameters.

Here, Fig. 1(a) shows the XRD pattern of the BGFO sample at room temperature. The preliminary analysis of the title compound was performed by using a computer-generated analysis software called X'Pert High Score Plus.[28] The XRD analysis shows that the sample has a rhombohedral (#*R*3*c*) crystal symmetry with cell parameters: $a = b = 5.5876$ Å, $c = 13.8670$ Å, $\alpha = \beta = 90°$, $\gamma = 120°$, volume (V) = 374.94 $Å^3$, and density = 8.31 g cm^{-3}, respectively (#$BiFeO_3$: JCPDS file no: 01-071-2494). Two weak secondary peaks of Gd_2O_3 are observed as shown in the XRD pattern [JCPDS file no: 00-012-0797 & 00-024-0430]. To understand the structural analysis better, Rietveld analysis was done, taking the $BiFeO_3$ CIF file: 2101912 as the input file. Fig. 1(b) shows the Rietveld fitting plot of the BGFO ceramic. It is observed that all peaks are fitted well, except for two Gd_2O_3 peaks. The recorded fitting parameters are R_{wp} (%) = 12.3621, R_b (%) = 9.6011, R_{exp} (%) = 7.4035 and σ = 1.67. Therefore, the presence of the Gd signal in the fitting of the pure $BeFeO_3$ ceramic confirms the formation of a solid solution of the $Bi_{0.9}Gd_{0.1}FeO_3$ ceramic and the obtained rhombohedral (#*R*3*c*) crystal symmetry.[22]

To calculate the average crystallite size and micro-lattice strain, we have usedthe Williamson–Hall (W–H) method. The mathematical relation for the W–H method can be written as: $\beta\cos\theta = 4\varepsilon\sin\theta + \frac{k\lambda}{D_{WH}}$, where all the symbols have their usual meaning.[29–31] Fig. 1(c) shows a $4\varepsilon\sin\theta$ *versus* $\beta\cos\theta$ plot of the BGFO ceramic. We can evaluate the slope and *y*-intercept for the final value of the lattice strain and average crystallite size. In the present study, the micro-lattice strain is found to be 1.06×10^{-3} [error bar = 8.94×10^{-4}], whereas the value of the average crystallite size (D) is found to be 65.5 nm [error bar = 1.17×10^{-3}]. We can calculate the average dislocation density (δ) using the relation $\delta = 1/D^2$, which is found to be 2.33×10^{14} m^{-2}.

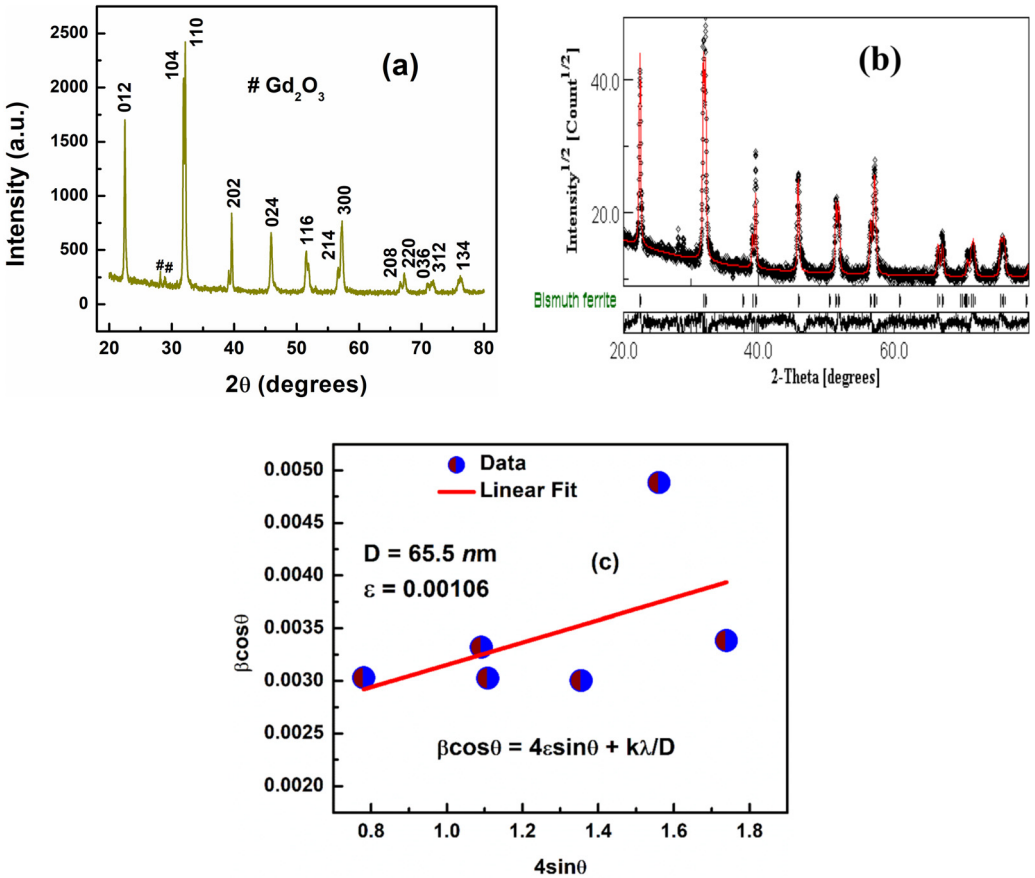

Fig. 1 (a) XRD pattern and (b) Rietveld fitting plot of the BGFO ceramic. (c) W–H plots of the BGFO ceramic.

3.3 FTIR study

Fig. 2 shows the FTIR spectrum of the BGFO ceramic at room temperature. The fingerprint region of the metal oxygen bond shows the characteristic absorption bands in the wavenumber region 400 to 600 cm^{-1}.[32] Hussain *et al.* (2022) show that metal–oxide stretching modes (Bi–O and Fe–O) in pure $BiFeO_3$ ceramics occur between 492 and 538 cm^{-1}.[33] The FTIR spectrum of pure $BiFeO_3$ displays two prominent absorption bands in the 400–1000 cm^{-1} region: ~527 cm^{-1}, corresponding to Fe–O stretching vibrations in FeO_6 octahedral units and ~821 cm^{-1}, attributed to higher-energy metal–oxygen vibrational modes associated with the perovskite *R3c* phase.

In the present study, upon Gd^{3+} doping (*e.g.*, $x = 0.1$), these bands shift slightly to ~535 cm^{-1} and ~827 cm^{-1}, respectively, confirming successful lattice incorporation.[34] Bi–O stretching vibrations typically appear in the low-frequency region near 440–460 cm^{-1}. In the present study, Fe–O bands are broad or intense, and they overlap and mask the weak Bi–O peaks.[34] Good doping levels are small; bands may be too weak to resolve. Gd–O (~440–460 cm^{-1}) coincides with strong Fe–O absorptions. Therefore, it can be concluded that the studied sample has all of the constituent metal-oxide vibration bands and complements the XRD analysis.

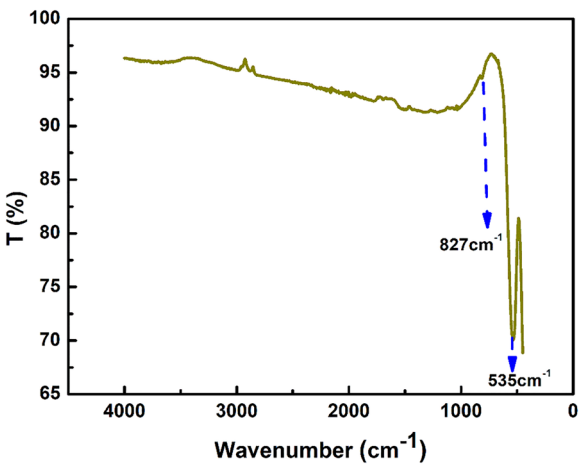

Fig. 2 The FTIR spectrum of the BGFO ceramic.

3.4 Optical property analysis

UV-Visible spectroscopy is essential for evaluating the optical absorption and bandgap energy of single perovskite materials, which directly influences their photovoltaic and optoelectronic performance. This technique helps identify transitions and defect states critical to optimizing device efficiency.[35,36] The absorption peak originates from an electronic transition in the molecule: when the photon energy matches the energy

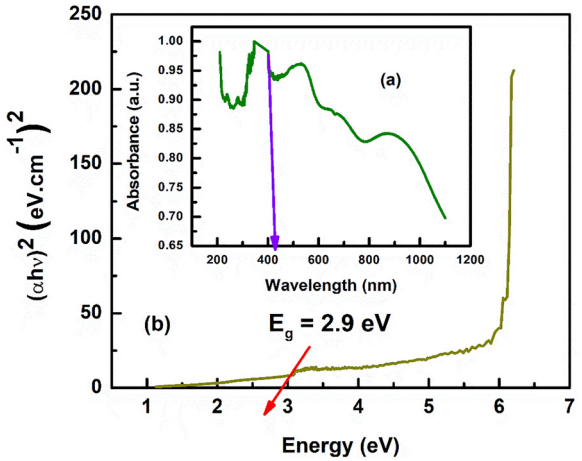

Fig. 3 (a) Absorbance *versus* wavelength, and (b) $(\alpha h\nu)^2$ *versus* the energy of the BGFO ceramic.

separation between the ground and excited states, efficient absorption occurs, producing a peak in the spectrum. The position and intensity of the peak reflect the molecular structure and its environment.

Fig. 3(a) illustrates the UV-visible absorption spectrum plotted as wavelength *versus* absorbance. The obtained optical data is analyzed using the Tauc relation, $(\alpha h\nu)^n = A(h\nu - E_g)$, where α is the absorption coefficient, $h\nu$ is the photon energy (eV), E_g is the optical bandgap energy, A is a constant, and the exponent $n = 2$ indicates a direct allowed transition.[37] The development of energy bands arises due to interactions between the charged ions of half-filled d-block cations, facilitating electronic transitions from the filled oxygen orbitals to the partially filled d-orbitals of transition metal ions. The bandgap energy of pure $BiFeO_3$ ceramic typically lies in the range of 2.1 to 2.8 eV, depending on factors such as synthesis method, grain size, and crystallinity.[38–40] Fig. 3(b) shows energy *versus* $(\alpha h\nu)^2$ of the BGFO ceramic. Extrapolation of the linear fit to the curve obtained between $h\nu$ *versus* $(\alpha h\nu)^2$ provides a bandgap of 2.9 eV, which is well-matched with the results from Fig. 3(a) and (b) as shown. Gadolinium (Gd^{3+}) doping in $BiFeO_3$ can cause an increase in the bandgap energy (*e.g.*, from ~2.3 eV to ~2.9 eV) due to two reasons: (i) Gd^{3+} ions (ionic radius ≈ 0.938 Å) substitute Bi^{3+} ions (≈ 1.03 Å), leading to lattice contraction and internal strain so that the Fe–O–Fe bond angles are reduced and the orbital overlap between Fe 3d and O 2p is modified, which affects the electronic band structure,[41,42] and (ii) Gd^{3+} substitution may alter local electric fields and the Fe^{3+}–O^{2-} bonding environment, shifting energy levels upward or downward, which modifies the conduction/valence band positions, possibly increasing the energy gap.[43]

3.5 Dielectric properties

Dielectric studies are essential for ceramic materials because they provide critical insights into polarization mechanisms, electrical insulation behavior, and energy storage capabilities, which are vital for applications in capacitors, sensors, memory devices, and high-frequency electronics.[44–47] To evaluate the dielectric constant (ε_r) and dielectric loss ($\tan\delta$) of ceramic compounds, a mathematical relation is used: $\varepsilon_r = Cd\varepsilon_0/A$ and $\tan\delta = \varepsilon''/\varepsilon'$, where all symbols have their usual meaning.[48] Fig. 4(a) shows the variation of dielectric constant *versus* frequency, whereas Fig. 4(b) shows the variation of $\tan\delta$ *versus* frequency of the BGFO ceramic at some selected temperatures. Polarization plays a key role in determining the dielectric properties of doped $BiFeO_3$, as doping can modify the strength and orientation of spontaneous polarization within the crystal. When polarization is enhanced or better aligned due to dopant-induced structural changes, the material exhibits higher dielectric permittivity and improved charge-storage capability. At the same time, doping can suppress unwanted polarization-related defects such as oxygen vacancies and domain wall pinning, which helps reduce dielectric loss and stabilizes the dielectric response across different frequencies. Overall, the interaction between polarization and dopant-induced lattice distortions is crucial for optimizing the dielectric performance of $BiFeO_3$-based ceramics.[49–51] In Gd-doped $BiFeO_3$ ceramics, the dielectric constant (ε') typically decreases with increasing frequency, which is attributed to the Maxwell–Wagner interfacial polarization and dipolar relaxation. At lower frequencies, space charge and grain boundary effects contribute to high dielectric values, while at higher frequencies, dipoles fail to follow the rapidly changing electric field, leading to reduced permittivity.[52]

Similarly, the $\tan\delta$ (dielectric loss) also decreases with frequency, indicating a reduction in energy dissipation due to delayed polarization processes. The high $\tan\delta$ at low frequencies is generally linked to defect-induced hopping conduction (*e.g.*, Fe^{3+}/Fe^{2+}), while its reduction at higher frequencies shows that the dielectric loss becomes minimal.[53] Fig. 4(c) shows the variation of dielectric constant *versus* temperature, whereas Fig. 4(d) shows the variation of $\tan\delta$ *versus* temperature of the BGFO ceramic at some selected frequencies. In Gd-doped $BiFeO_3$ ceramics, the dielectric constant (ε') increases with rising temperature, especially near the ferroelectric–paraelectric transition temperature of 390 °C, due to enhanced thermal activation of dipoles and increased space charge polarization. This behavior is typical for ferroelectric materials, where higher thermal energy allows dipoles to reorient more easily, leading to an increase in permittivity.[54,55] The $\tan\delta$ also increases with temperature, mainly because of the enhanced mobility of charge carriers and leakage current at higher temperatures. A distinct peak in $\tan\delta$ may appear near 290 °C, indicating a relaxation process.[56,57] The shift of the relaxation peak in $\tan\delta$ with increasing temperature indicates a thermally activated relaxation process, where dipoles or charge carriers require less energy to reorient at higher temperatures, causing the loss peak to move toward lower frequencies or higher temperatures, depending on the relaxation mechanism.

3.6 Impedance analysis

Impedance spectroscopy is essential for $BiFeO_3$ ceramics as it provides critical insights into their electrical conduction mechanisms, grain and grain boundary contributions, and

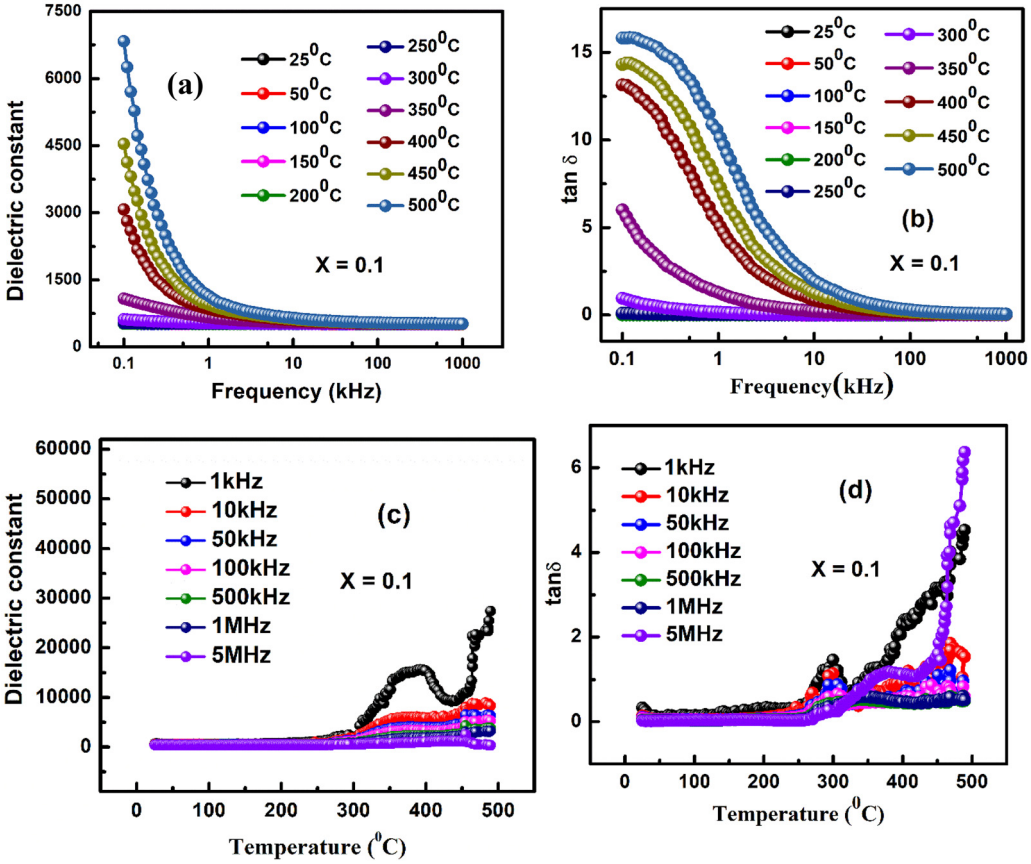

Fig. 4 (a) The dielectric constant *versus* frequency, (b) tan δ *versus* frequency, (c) dielectric constant *versus* temperature, and (d) tan δ *versus* temperature of the BGFO ceramic.

dielectric relaxation behavior, which are key for optimizing their multiferroic and functional properties. Fig. 5(a) and (b) show the variation of real (Z') and imaginary (Z'') components of impedance with frequency. Z' shows a decreasing trend with frequency, indicating enhanced conductivity due to reduced grain boundary resistance at higher frequencies. It supports the semiconducting nature of the sample under study.[58]

The Z'' *versus* frequency plots for BGFO exhibit one or more characteristic peaks, whose positions shift toward higher frequencies as temperature increases, indicating thermally activated relaxation processes.[59] Fig. 5(c) shows the graph of Z' *versus* Z'' of the BGFO ceramic at some selected temperatures. The radius of the semicircular arcs decreases with the rise of temperature, supporting the semiconducting maturity of the sample.[60]

3.7 Modulus analysis

Modulus study is required for ceramics to analyze dielectric relaxation and distinguish between electrode effects and bulk material responses, offering deeper insight into charge carrier dynamics and localized conduction processes. The complex electric modulus M^* is related to the complex permittivity ε^* by: $M^* = 1/\varepsilon^* = M' + iM''$, where $\varepsilon^* = \varepsilon' - i\varepsilon'''$, $M' = \varepsilon'/[(\varepsilon')^2 + (\varepsilon'')^2]$, $M'' = \varepsilon''/[(\varepsilon')^2 + (\varepsilon'')^2]$, M' = real part of the modulus (storage modulus) and M'' = imaginary part (loss modulus), indicating relaxation processes.[61,62] Fig. 6(a) and (b) show the variation of M' with frequency and M'' *versus* frequency at some selected temperatures. At lower frequencies, the M' values are nearly zero and coincide across compositions, indicating negligible electrode polarization; as frequency increases, M' gradually rises and plateaus at high frequency, reflecting the transition from long-range conduction to localized charge relaxation and confirming non-Debye–type behavior in the material.[63] In the present study, the imaginary modulus M'' exhibits broad peaks whose relaxation frequency (f_n) shifts to higher frequencies with both increasing temperature and 10% Gd content. These peaks are asymmetric and broadened, indicating a distribution of relaxation times and non-Debye-type relaxation behavior, typically associated with localized hopping of charge carriers within grains or across grain boundaries.[64]

Cole–Cole plots help identify and distinguish grain and grain boundary responses through separate semicircular arcs, revealing resistive and capacitive behavior of different microstructural regions in polycrystalline BGFO ceramics. Fig. 6(c) shows the Cole–Cole plots of the BGFO ceramic at some selected temperatures. The presence of the semicircular arcs in the Cole–Cole plots confirms the semiconducting nature.[65]

3.8 AC conductivity study

The study of ac conductivity in Gd-doped $BiFeO_3$ ceramics is essential to understand the frequency-dependent charge

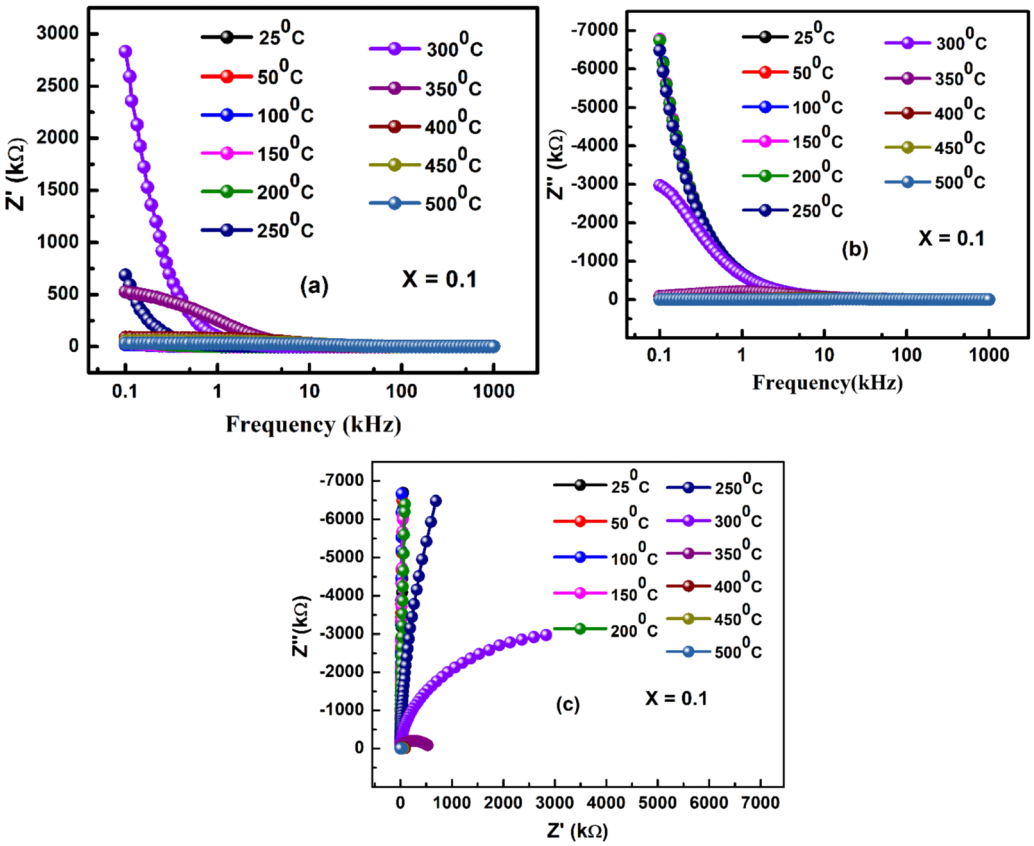

Fig. 5 (a) The Z' *versus* frequency, (b) Z'' *versus* frequency, and (c) Z' *versus* Z'' of the BGFO ceramic.

transport mechanisms and assess the influence of Gd doping on electrical conduction behavior.

The ac conductivity can be calculated from the dielectric data as: $\sigma_{ac}(\omega) = \varepsilon_0 \omega \tan\delta$, where ε_0 = permittivity of free space (8.854×10^{-12} F m^{-1}), $\tan\delta$ = dielectric loss, and $\omega = 2\pi f$ = angular frequency.[66] Fig. 7(a) shows the ac conductivity *versus* frequency at some selected temperatures. At low frequencies, σ_{ac} remains nearly frequency-independent, forming a plateau corresponding to σ_{dc} (dc conductivity), a regime dominated by long-range charge transport across grains. As frequency increases, σ_{ac} begins to rise following Jonscher's universal power law, *i.e.*, $\sigma_{ac} = \sigma_{dc} + A\omega^n$, where exponent n ($0 < n < 1$) and pre-exponential factor A reveal a hopping conduction mechanism involving small polarons or localized charge carriers.[67] As the temperature rises or when Gd concentration reaches 10%, the dispersion begins at lower frequencies and the slope parameter (n) decreases, suggesting improved charge carrier mobility and a lower activation energy for hopping conduction. Fig. 7(b) shows ac conductivity *versus* $1000/T$ at some selected frequencies. Temperature-dependent ac conductivity obeys the Arrhenius relationship: $\sigma_{ac} = \sigma_0 e^{-\frac{E_a}{k_B T}}$, where E_a = activation energy, and k_B = Boltzmann's constant = 1.38×10^{23} J K^{-1}.[68] The activation energy values are calculated from the slope of $\ln(\sigma)$ *vs.* $1/T$ plots. The calculated values of the activation energy are 0.511 eV, 0.384 eV, 0.257 eV, 0.186 eV, 0.167 eV, 0.158 eV, and 0.151 eV at 1 kHz, 10 kHz, 100 kHz, 300 kHz, 500 kHz, 700 kHz, and 1 MHz, respectively. The gradual decrease in activation energy with increasing frequency suggests that charge carriers require less energy to hop at higher frequencies, supporting a thermally activated conduction process.[69]

3.9 Thermistor behaviour

Thermistor studies in ceramics are essential to evaluate their temperature-dependent resistive behavior, enabling their application in temperature sensing and thermal protection devices. Fig. 8(a) shows the variation of resistance *versus* temperature, while Fig. 8(b) shows the variation of $\ln R$ *versus* $1/T$ of the BGFO ceramic. Thermistive materials fall into two primary categories: NTCR, where resistance decreases with rising temperature, and PTCR, where the opposite occurs. In the present study, the nature of NTCR and PTCR of BGFO was analyzed in depth. Resistance data were extracted from Nyquist plots generated *via* complex impedance spectroscopy, across a temperature range from 300 K to 800 K in steps of 25 K. Plotting these resistance values against temperature revealed a consistent downward trend from 300 to 500 °C, affirming the NTC thermistor character of the sample.[70] Additionally, a graph of $\ln(R)$ *versus* $1/T$ further confirmed this thermally activated semiconducting behavior, an indication that increased thermal energy facilitates carrier excitation and movement, thereby reducing resistance.[71] Fig. 8(c) shows the variation of the thermistor constant *versus* temperature. To quantify this thermistor

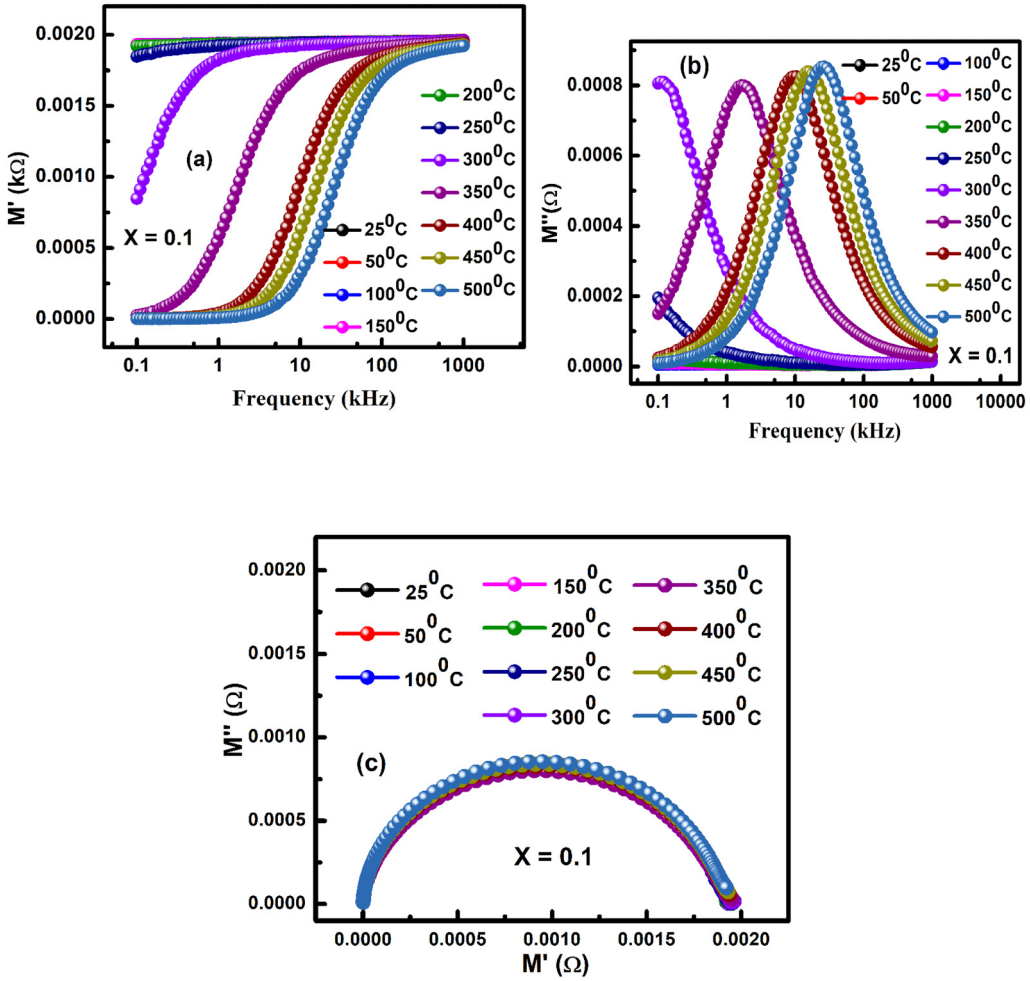

Fig. 6 (a) M' *versus* frequency, (b) M'' *versus* frequency, and (c) M' *versus* M'' of the BGFO ceramic.

behavior, the thermistor constant (β) was calculated using resistance values at two adjacent temperatures, based on the following empirical relation: $\beta = \ln\left(\frac{R_1}{R_2}\right) \Big/ \left(\frac{1}{T_1} - \frac{1}{T_2}\right)$, where R_1 and R_2 are the resistances at absolute temperatures T_1 and T_2, respectively.[72]

This parameter provides insight into how sharply resistance changes with temperature. The calculated β values ranged from 2334 K to 4406 K, depending on the specific temperature interval. According to established criteria, β values between 2000 K and 5000 K are typically associated with low-temperature thermistors, while much higher values are characteristic of high-temperature

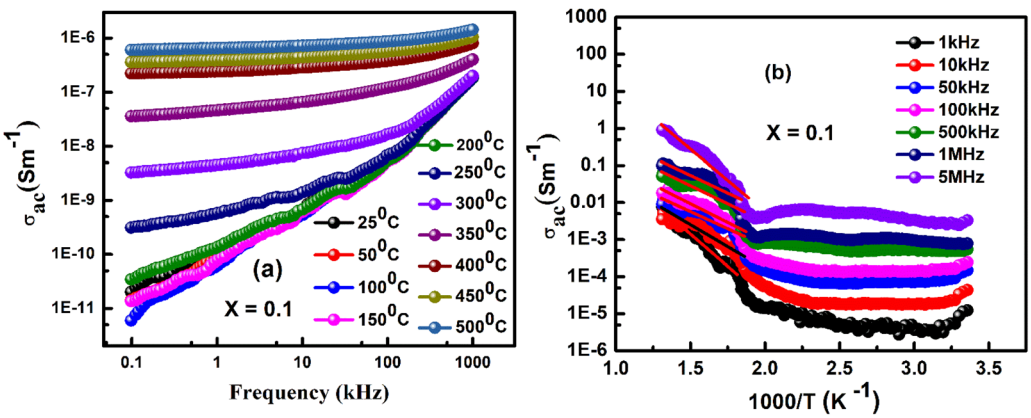

Fig. 7 (a) and (b) The ac conductivity *versus* frequency and the ac conductivity *versus* 1000/T of the BGFO ceramic.

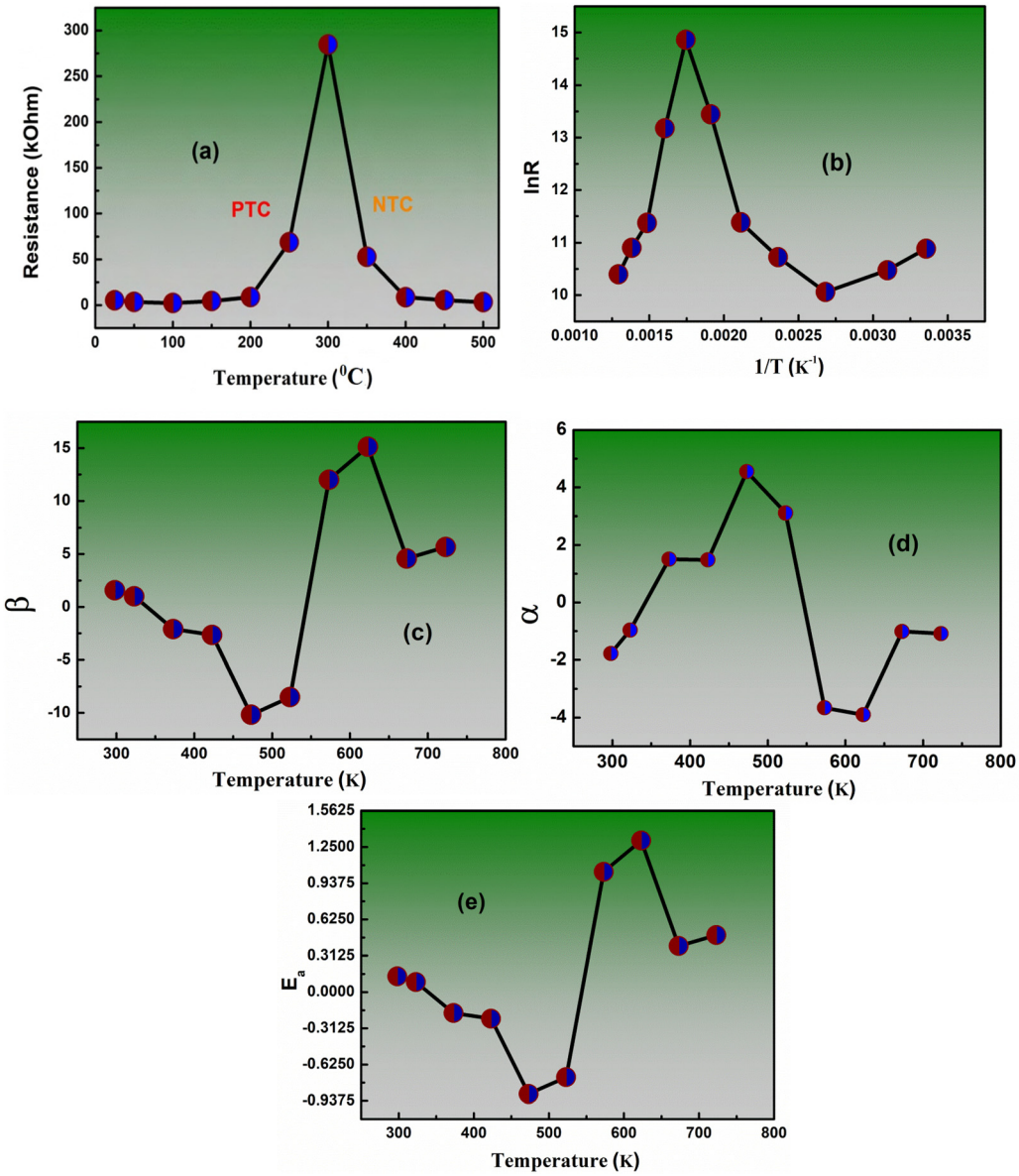

Fig. 8 (a) Resistance *versus* temperature, (b) ln *R versus* 1/*T*, (c) thermistor constant *versus* temperature, (d) sensitivity factor *versus* temperature, and (e) activation energy *versus* temperature of the BGFO ceramic.

sensing materials. Therefore, the β values observed for BGFO suggest strong potential for high-temperature thermistor applications.

Another significant performance metric is the sensitivity factor (α), which measures the relative rate of resistance change with temperature. It is calculated using: $\alpha = \left(\frac{-\beta}{T^2}\right) \times 100$, where α is the sensitivity in percentage per Kelvin, β is the thermistor constant, and T is the absolute temperature in Kelvin.[73] This relationship shows that sensitivity increases with higher β and decreases with rising temperature. The plot in Fig. 8(d) shows an inverse nonlinear relationship, indicating that sensitivity gradually declines as temperature increases, a hallmark of NTC thermistor behavior. This trend reflects reduced responsiveness at elevated temperatures, which aligns with theoretical expectations.

The observed thermal behavior can be attributed to the crystal structure of BGFO, particularly the octahedral coordination of transition metal cations at the B-site with surrounding oxygen anions. These structural features facilitate charge transfer through partially filled d-orbitals, enhancing mobility and improving thermistor efficiency. Finally, the activation energy (E_a) corresponding to the thermally driven conduction was calculated from the thermistor constant using: $E_a = k_B \times \beta$, where E_a is the activation energy in eV, β is the thermistor constant, and k_B is Boltzmann's constant (8.617×10^{-5} eV K^{-1}).[74,75] The activation energy values, plotted as a function of temperature, mirrored the trend of β, consistent with their direct proportional relationship as shown in Fig. 8(e). These moderate activation energies support the presence of easily excitable charge carriers, further confirming the semiconducting and NTC thermistor characteristics in the high temperature range.

4. Conclusion

In this communication, a comprehensive study on the structural, dielectric, electrical, and optical properties of the Gd-doped $BiFeO_3$ ceramic is presented. The preliminary structural analysis by MADU Rietveld refinement confirms that the BGFO ceramic has a rhombohedral structure with an average crystallite size of 65.5 nm, micro-lattice strain of 0.00106, and dislocation density of 2.33×10^{14} m^{-2}. The analysis of the FTIR spectrum confirms the presence of a wide and strongly intense vibration band of Fe–O at 535 cm^{-1}, and two other weak bands of Bi–O and Gd–O are overlapped with the Fe–O stretching band. So, our prepared sample has all constituent elements and this is supported by the results of the XRD analysis. The analysis of the UV-visible data provides the bandgap energy of 2.9 eV, supporting the application for photodetectors and light-detecting devices. A wide range of dispersed values of dielectric constant and loss are observed at low frequency due to the strong effect of dipolar and space charge polarization. Interestingly, with the rise of frequency, both the dielectric constant and loss decrease due to the reduction of space charge polarization. The study of impedance plots *versus* frequency confirms the presence of semiconducting and relaxation behaviour. Again, the study of modulus plots with frequency confirms a non-Debye type of relaxation mechanism in the studied sample. AC conductivity studies suggest a thermally activated hopping process that controls the whole conductivity mechanism in the sample. The study of resistance *versus* temperature plots confirms the semiconducting nature, and analysis of the thermistor coefficient *versus* temperature confirms the NTC thermistor character at high temperature.

Author contributions

Swati Panda: data curation, writing – original draft, conceptualization, and methodology, and S. K. Parida: validation, software, writing – reviewing and editing, visualization, and supervision.

Conflicts of interest

There are no conflicts of interest to declare.

Data availability

Data will be made available upon reasonable request.

Acknowledgements

There is no funding for the preparation of the presented work. The authors would like to thank the host Institute for the XRD characterization.

References

1 J. H. Noh, S. H. Im, J. H. Heo, T. N. Mandal and S. I. Seok, Chemical management for colorful, efficient, and stable inorganic–organic hybrid nanostructured solar cells, *Nano Lett.*, 2013, **13**, 1764–1769.
2 M. Saliba, T. Matsui, J. Y. Seo, K. Domanski, J. P. Correa-Baena, M. K. Nazeeruddin and M. Grätzel, Cesium-containing triple cation perovskite solar cells: improved stability, reproducibility, and high efficiency, *Energy Environ. Sci.*, 2016, **9**, 1989–1997.
3 A. Kojima, K. Teshima, Y. Shirai and T. Miyasaka, Organometal halide perovskites as visible-light sensitizers for photovoltaic cells, *J. Am. Chem. Soc.*, 2009, **131**, 6050–6051.
4 S. D. Stranks and H. J. Snaith, Metal–halide perovskites for photovoltaic and light-emitting devices, *Nat. Nanotechnol.*, 2015, **10**, 391–402.
5 Z. K. Tan, R. S. Moghaddam, M. L. Lai, P. Higler, R. Docampo, F. Deschler and R. H. Friend, Bright light-emitting diodes based on organometal halide perovskite, *Nat. Nanotechnol.*, 2014, **9**, 687–692.
6 L. Dou, Y. M. Yang, J. You, Z. Hong, W. H. Chang, G. Li and Y. Yang, Solution-processed hybrid perovskite photodetectors with high detectivity, *Nat. Commun.*, 2014, **5**, 5404.
7 M. Saliba, T. Matsui, J. Y. Seo, K. Domanski, J. P. Correa-Baena, M. K. Nazeeruddin and M. Grätzel, Cesium-containing triple cation perovskite solar cells: improved stability, reproducibility, and high efficiency, *Energy Environ. Sci.*, 2016, **9**, 1989–1997.
8 S. Supriya, Recent trends and morphology mechanisms of rare-earth based $BiFeO_3$ nano perovskites with excellent photocatalytic performances, *J. Rare Earths*, 2023, **41**, 331–341.
9 D. Dash, A. Palai and D. Sahu, Nanocrystalline gadolinium doped ZnO: an excellent photoluminescent material and efficient photocatalyst towards optoelectronic and environment remedial applications, *Ceram. Int.*, 2022, **48**, 28835–28842.
10 R. Balakrishnan, A. Dixit, R. Naik and M. S. R. Rao, Enhancement in electrical and magnetodielectric properties of Ca- and Ba-doped $BiFeO_3$ polycrystalline ceramics, *J. Am. Ceram. Soc.*, 2018, **101**, 782–788.
11 A. Palai, N. Ranjan Panda, S. Chhotaray and D. Sahu, Sm doped ZnO-SnO_2 nanocomposites with improved photodegradation strength and antibacterial properties, *Surf. Interfaces*, 2023, **41**, 103217.
12 D. Sahu, N. R. Panda and B. S. Acharya, Effect of Gd doping on structure and photoluminescence properties of ZnO nanocrystals, *Mater. Res. Express*, 2017, **4**, 114001.
13 P. Banerjee and A. Franco Júnior, Rare earth and transition metal doped $BiFeO_3$ ceramics: structural, magnetic and dielectric characterization, *J. Mater. Sci.: Mater. Electron.*, 2016, **27**, 6053–6059.
14 J. Wang, J. B. Neaton, H. Zheng, V. Nagarajan, S. B. Ogale, B. Liu and R. Ramesh, Epitaxial $BiFeO_3$ multiferroic thin film heterostructures, *Science*, 2003, **299**, 1719–1722.
15 Q. Wu, Y. Song, C. Jia, Z. Gao and W. Zhang, Effect of Nd and Mn Co-Doping on Dielectric, Ferroelectric and Photovoltaic Properties of $BiFeO_3$, *Crystals*, 2022, **12**, 500.
16 T. J. Park, G. C. Papaefthymiou, A. J. Viescas, A. R. Moodenbaugh and S. S. Wong, Size-dependent

magnetic properties of single-crystalline multiferroic $BiFeO_3$ nanoparticles, *Nano Lett.*, 2007, **7**, 766–772.
17 M. Kumar and K. L. Yadav, Large dielectric and weak ferromagnetic behavior of $BiFeO_3$ ceramics synthesized using Fe_2O_3 nanopowder, *J. Phys. D: Appl. Phys.*, 2007, **40**, 5317–5320.
18 A. Singh, B. C. Yadav and R. S. Tiwari, Enhancement of multiferroic properties in rare-earth substituted $BiFeO_3$, *J. Alloys Compd.*, 2014, **615**, 877–884.
19 S. K. Singh, R. S. Katiyar and J. F. Scott, Optical properties and Raman scattering of multiferroic $BiFeO_3$ thin films, *J. Appl. Phys.*, 2008, **103**, 074103.
20 A. Singh, B. C. Yadav and R. S. Tiwari, Structural, dielectric, and magnetic properties of Gd-doped $BiFeO_3$ multiferroic ceramics, *J. Alloys Compd.*, 2014, **615**, 877–884.
21 V. A. Khomchenko, D. A. Kiselev, J. M. Vieira, A. L. Kholkin and P. M. Vilarinho, Effect of rare-earth substitution on the structure and multiferroic properties of $BiFeO_3$ ceramics, *J. Appl. Phys.*, 2008, **103**, 024105.
22 D. K. Pradhan, P. R. Das, R. N. P. Choudhary and S. Das, Dielectric and magnetic properties of Gd-modified $BiFeO_3$ multiferroic ceramics, *Mater. Chem. Phys.*, 2013, **139**, 609–615.
23 D. Kothari, G. Sharma and R. K. Kotnala, Enhanced magnetic and dielectric properties of Gd-doped $BiFeO_3$ nanoparticles, *Mater. Res. Bull.*, 2011, **46**, 1837–1842.
24 S. K. Mendiratta, R. Kumar and R. K. Dwivedi, Improved dielectric and ferroelectric behavior of Gd-doped $BiFeO_3$ ceramics, *J. Mater. Sci.: Mater. Electron.*, 2016, **27**, 7392–7400.
25 V. M. Goldschmidt, Die gesetze der krystallochemie, *Naturwissenschaften*, 1926, **14**, 477–485.
26 R. D. Shannon, Revised Effective Ionic Radii and Systematic Studies of Interatomic Distances in Halides and Chalcogenides, *Acta Crystallogr., Sect. A*, 1976, **32**, 751–767.
27 C. J. Bartel, C. Sutton, B. R. Goldsmith, R. Ouyang, C. B. Musgrave, L. M. Ghiringhelli and M. Scheffler, New tolerance factor to predict the stability of perovskite oxides and halides, *Sci. Adv.*, 2019, **5**, eaav0693.
28 M. Padhi, S. Mishra, A. Prasad Sahu and S. K. Parida, A comprehensive study on the structure, microstructure, dielectric, electrical, and infrared properties of the BiNaCo-MoO_6 ceramic for NTC thermistor applications, *J. Mater. Sci.: Mater. Electron.*, 2025, **36**, 1966.
29 G. K. Williamson and W. H. Hall, X-ray line broadening from fielded aluminum and wolfram, *Acta Metall.*, 1953, **1**, 22–31.
30 S. Mishra and S. K. Parida, Electrical and optical properties of a lead-free complex double perovskite $BaNaFeMoO_6$: photovoltaic and thermistor applications, *Mater. Sci. Eng., B*, 2023, **296**, 116629–116645.
31 M. G. Hajiabadi, M. Zamanian and D. Souri, Williamson-Hall analysis in evaluation of lattice strain and the density of lattice dislocation for nanometer-scaled ZnSe and ZnSe:Cu particles, *Ceram. Int.*, 2019, **45**, 14084–14089.
32 A. Hezam, K. Namratha, Q. A. Drmosh, Z. H. Yamani and K. Byrappa, Synthesis of Heterostructured Bi_2O_3–CeO_2–ZnO Photocatalyst with Enhanced Sunlight Photocatalytic Activity, *Ceram. Int.*, 2017, **43**, 5292–5301.
33 G. Hussain, I. Ahmed, A. U. Rehman, M. U. Subhani, N. Morley and M. Akhtar, *et al.*, Study of the role of dysprosium substitution in tuning structural, optical, electrical, dielectric, ferroelectric, and magnetic properties of bismuth ferrite multiferroic, *J. Alloys Compd.*, 2022, **919**, 165743.
34 S. R. Dhanya, S. G. Nair, J. Satapathy and N. Pavan Kumar, Structural and spectroscopic characterization of bismuth-ferrites, *AIP Conf. Proc.*, 2019, **2166**, 020017.
35 J. H. Heo, *et al.*, Efficient inorganic–organic hybrid heterojunction solar cells containing perovskite compound and polymeric hole conductors, *Nat. Photonics*, 2013, **7**, 486–491.
36 G. Xing, *et al.*, Long-range balanced electron- and hole-transport lengths in organic-inorganic $CH_3NH_3PbI_3$, *Science*, 2013, **342**, 344–347.
37 J. Tauc, R. Grigorovici and A. Vancu, Optical properties and electronic structure of amorphous germanium, *Phys. Status Solidi B*, 1966, **15**, 627–637.
38 G. Catalan and J. F. Scott, Physics and applications of bismuth ferrite, *Adv. Mater.*, 2009, **21**, 2463–2485.
39 S. M. Selbach, *et al.*, Band gap and electronic structure of $BiFeO_3$ from hybrid functional and O 1s X-ray absorption spectroscopy, *J. Solid State Chem.*, 2012, **196**, 249–254.
40 R. Mazumder, *et al.*, Structural, optical and magnetic properties of sol–gel synthesized $BiFeO_3$ ceramics, *Ceram. Int.*, 2014, **40**, 10459–10466.
41 M. Selvakumar, *et al.*, Influence of rare earth doping on structural, optical and magnetic properties of $BiFeO_3$ nanoparticles, *J. Alloys Compd.*, 2011, **509**, 9800–9806.
42 A. Sharma, *et al.*, Influence of Gd doping on structure, bandgap, and magnetic properties of $BiFeO_3$ ceramics, *Ceram. Int.*, 2016, **42**, 13847–13854.
43 Q. Liu, *et al.*, Enhanced multiferroic properties and band-gap tuning in Gd-doped $BiFeO_3$ ceramics, *J. Mater. Sci.: Mater. Electron.*, 2016, **27**, 10758–10765.
44 M. M. Kumar, A. Srinivas and S. V. Suryanarayana, Structure–property relation in Nd-substituted $BiFeO_3$, *J. Appl. Phys.*, 2000, **87**, 855–862.
45 S. Ghosh and R. N. P. Choudhary, Impedance and dielectric studies of $BiFeO_3$–$PbTiO_3$ ceramics, *Mater. Chem. Phys.*, 2009, **114**, 44–49.
46 P. Lunkenheimer, *et al.*, Origin of apparent colossal dielectric constants, *Phys. Rev. B: Condens. Matter Mater. Phys.*, 2002, **66**, 052105.
47 S. Suthar, *et al.*, Dielectric and impedance analysis of rare earth doped $BiFeO_3$ ceramics, *Ceram. Int.*, 2016, **42**, 12529–12536.
48 B. Kumar Vashisth, J. S. Bangruwa, S. P. Gairolaa and V. Verma, Structural, dielectric, ferroelectric, and magnetic properties of doped $BiFeO_3$, *Integr. Ferroelectr.*, 2018, **194**, 21–27.
49 N. Ranjan Panda, S. K. Sahu, A. Palai, T. Yadav, D. Behera and D. Sahu, Unraveling the synergistic effects in ZnO–MoS_2 nanocomposite leading to enhanced photocatalytic,

antibacterial, and dielectric characteristics, *Chem. Phys. Impact*, 2024, **8**, 100550.
50 D. Sahu and N. Ranjan Panda, Synthesis of novel nanocomposite of g-C_3N_4 coated ZnO–MoS_2 for energy storage and photocatalytic applications, *Chemosphere*, 2024, **350**, 141014.
51 Y. Saad, I. Álvarez-Serrano, M. L. López and M. Hidouri, Dielectric response and thermistor behavior of lead-free xNaNbO$_3$ − (1 − x)BiFeO$_3$ electroceramics, *Ceram. Int.*, 2018, **44**, 18560–18570.
52 S. Ghosh, *et al.*, Dielectric relaxation and AC conductivity in Gd-modified $BiFeO_3$ ceramics, *J. Alloys Compd.*, 2011, **509**, 7584–7592.
53 A. K. Jonscher, The 'universal' dielectric response, *Nature*, 1977, **267**, 673–679.
54 S. Suthar, Y. Sharma and N. Ahlawat, Dielectric and impedance analysis of rare earth doped $BiFeO_3$ ceramics, *Ceram. Int.*, 2016, **42**, 12529–12536.
55 M. K. Singh, R. S. Katiyar and J. F. Scott, New magnetic phase transitions in $BiFeO_3$, *J. Phys.: Condens. Matter*, 2008, **20**, 252203.
56 M. M. Kumar, A. Srinivas and S. V. Suryanarayana, Structure–property relation in Nd-substituted $BiFeO_3$, *J. Appl. Phys.*, 2000, **87**, 855–862.
57 K. L. Yadav, Dielectric and magnetic behavior of multiferroic $BiFeO_3$ ceramics, *J. Phys. D: Appl. Phys.*, 2008, **41**, 135005.
58 A. Khanna, *et al.*, Structural, dielectric and magnetic properties of Gd-doped $BiFeO_3$ ceramics, *Mater. Res. Bull.*, 2013, **48**, 3907–3913.
59 S. K. Parida, P. K. Das and R. N. P. Choudhary, Structural and Electrical Characterization of $SrMn_{0.97}Ce_{0.03}O_3$ Ceramics, *Integr. Ferroelectr.*, 2021, **221**, 215–230.
60 S. Mishra and S. K. Parida, Lead-free complex double perovskite $SrLiFeWO_6$: structural, microstructure, electrical and optical study, *Phys. B*, 2023, **668**, 415246.
61 T. Md Rahman, M. Vargas and C. V. Ramana, structural characteristics, electrical conduction, and dielectric properties of gadolinium-substituted cobalt ferrite, *J. Alloys Compd.*, 2014, **617**, 547–562.
62 Y. D. Kolekar, *et al.*, Impedance spectroscopy and modulus studies of $BiFeO_3$ ceramics, *J. Alloys Compd.*, 2011, **509**, 942–948.
63 S. Kumar, *et al.*, Effect of Nd Doping on Structural, Electrical and Optical Properties of $BiFeO_3$ Ceramics, *Ceram. Int.*, 2017, **43**, 14859–14867.
64 S. Pattanayak, B. N. Parida, P. R. Das and R. N. P. Choudhary, Impedance spectroscopy of Gd-doped $BiFeO_3$ multiferroics, *Appl. Phys. A*, 2013, **112**, 387–395.
65 S. Mishra, R. N. P. Choudhary and S. K. Parida, Structural, dielectric, electrical, and optical properties of a double perovskite: $BaNaFeWO_6$ for some device applications, *J. Mol. Struct.*, 2022, **1265**, 133353.
66 S. Mishra and S. K. Parida, Investigation of structure, dielectric, thermistor, and optical properties study of an eco-friendly double perovskite for photovoltaic and optoelectronic applications: $CaLiFeWO_6$, *Curr. Appl. Phys.*, 2024, **65**, 75–90.
67 R. Das and R. N. P. Choudhary, Studies of structural, dielectric relaxation and impedance spectroscopy of lead-free double perovskite: Dy_2NiMnO_6, *J. Mater. Sci.: Mater. Electron.*, 2018, **29**, 19099–19110.
68 A. Goswami and P. K. Mahapatra, Impedance spectroscopy and Cole–Cole analysis of dielectric properties in lead-based ceramic materials, *Ceram. Int.*, 2014, **40**, 7291–7300.
69 R. Kumar and S. B. Rai, Electrical and Dielectric Properties of Ferrite Ceramics Through Nyquist Plot Interpretation, *J. Mater. Sci.: Mater. Electron.*, 2017, **28**, 7893–7900.
70 S. Mishra and S. K. Parida, Lead-free complex double perovskite $SrLiFeWO_6$: structural, microstructure, electrical and optical study, *Phys. B*, 2023, **668**, 415246.
71 S. Mishra and S. K. Parida, Electrical and optical properties of a lead-free complex double perovskite $BaNaFeMoO_6$: photovoltaic and thermistor applications, *Mater. Sci. Eng., B*, 2023, **296**, 116629–116645.
72 S. Sahoo, Enhanced time response and temperature sensing behavior of thermistor using Zn-doped $CaTiO_3$ nanoparticles, *J. Adv. Ceram.*, 2018, **7**, 99–108.
73 D. Saha, A. Das Sharma, A. Sen and H. S. Maiti, Preparation of bixbyite phase $(Mn_xFe_{1-x})_2O_3$ for NTC thermistor applications, *Mater. Lett.*, 2002, **55**, 403–406.
74 F. C. S. Luz, S. A. Pianaro, C. E. Yurk, G. Capobianco, A. J. Zara and S. M. Tebcherani, Construction and testing of a system for the electrical characterization of ceramic thermistors at low temperatures, *Ceramica*, 2014, **60**, 96–101.
75 A. Feteira, Negative Temperature Coefficient Resistance (NTCR) Ceramic Thermistors: An Industrial Perspective, *J. Am. Ceram. Soc.*, 2009, **92**, 967–983.